Supplemental Data

Anti-microRNA-21 prevents progression of Alport syndrome by stimulating metabolic pathways

Ivan G. Gomez[1], Deidre A. MacKenna[2], Bryce G. Johnson[1,7], Vivek Kaimal[2], Allie M. Roach[1,7], Shuyu Ren[1,7], Naoki Nakagawa[1], Cuiyan Xin[1], Rick Newitt[1], Shweta Pandya[2], Tai-He Xia[3] Xueqing Liu[2], Dorin-Bogdan Borza[4], Monica Grafals[5], Stuart J. Shankland[1], Jonathan Himmelfarb[1], Didier Portilla[6], Shiguang Liu[3], B. Nelson Chau[2], and Jeremy S. Duffield[1,7]

1. Supplemental Figures

Figure S1

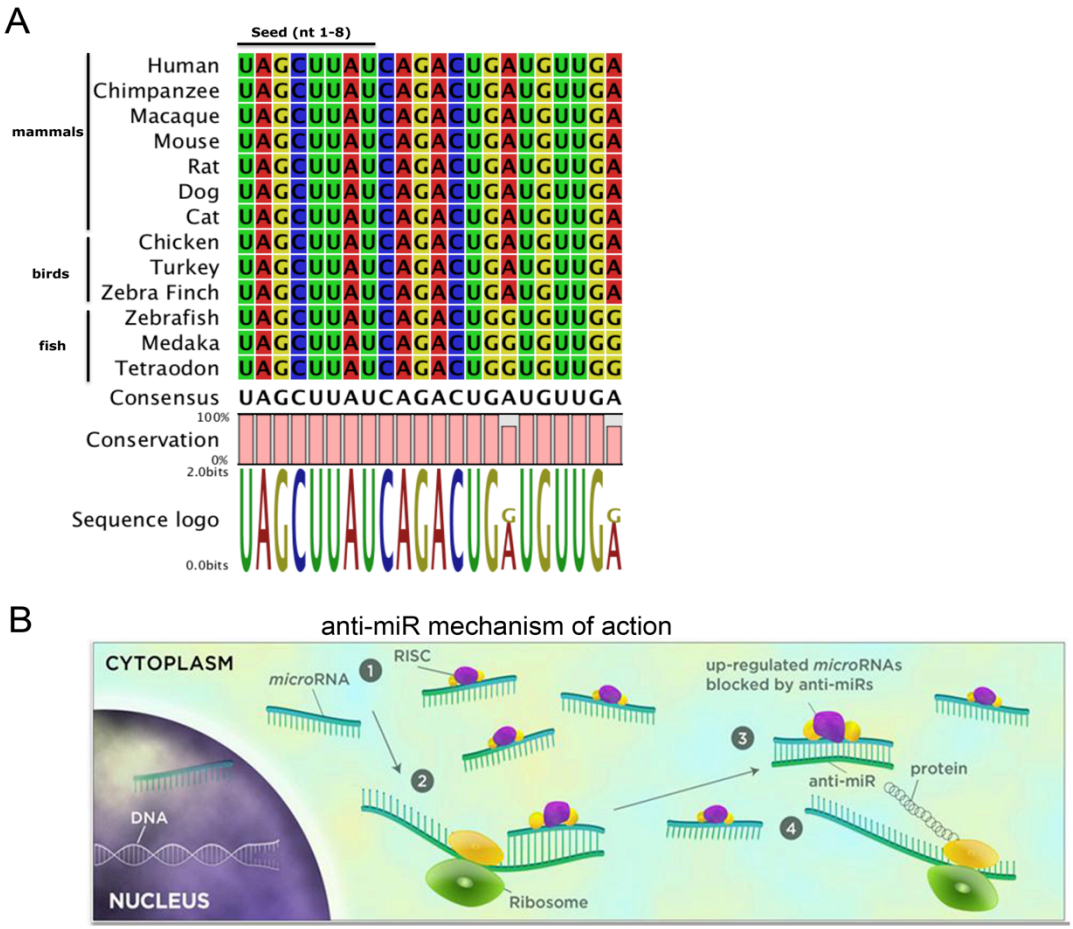

Supplemental Figure 1.

miR-21 is highly conserved across species and its activity is inhibited by ant-microRNA oligonucleotides. (A) The sequence of mature miR-21-5p is shown for different mammalian species and determined by CLC Genomics Workbench analysis. The 5' octamer, critical for binding to and silencing mRNA is represented by the first 8 nucleotides. (B) Schematic showing mechanism by which anti-miR21 oligonucleotides silence mRNA. Anti-miR freely enters the cells where is binds to the specific mature miRNA loaded in the Argonaut complex by sequence complementarity, thereby preventing interaction of the miR with its target mRNAs.

Figure S2

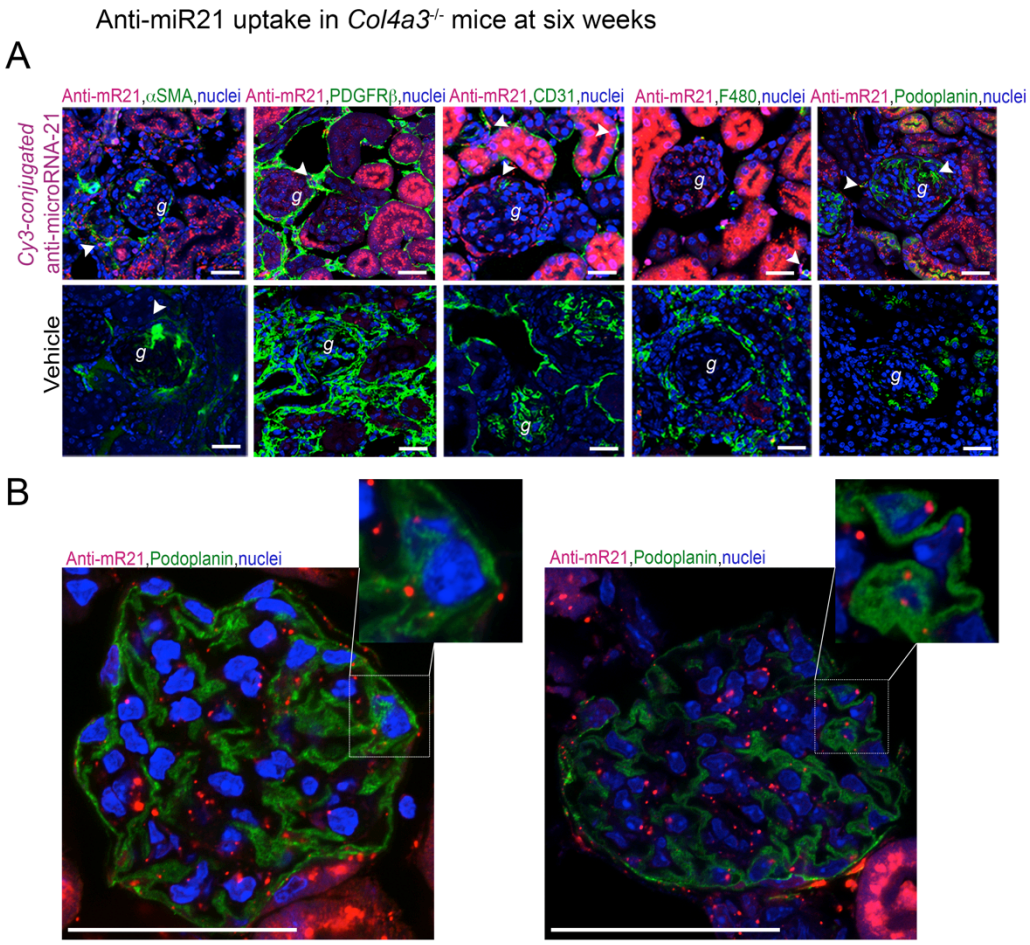

Supplemental Figure 2.

Distribution of anti-miR21-Cy3 in kidneys. (A) Images showing distribution of anti-miR21 (red) to kidneys of 6 week old *Col4a3*$^{-/-}$ mice, 48h following a single dose of anti-miR-21 subcutaneously. Note widespread distribution to tubules but also glomeruli (g). Anti-miR-21 can be seen in PDGFRβ+ fibroblasts, αSMA+ myofibroblasts and podoplanin+ podocytes (arrowheads) (bar = 50μm). (B) Images showing podocytes stained with podoplanin in 6 week old *Col4a3*$^{-/-}$ mice indicating uptake of anti-miR21-Cy3 (bar = 50μm).

Figure S3

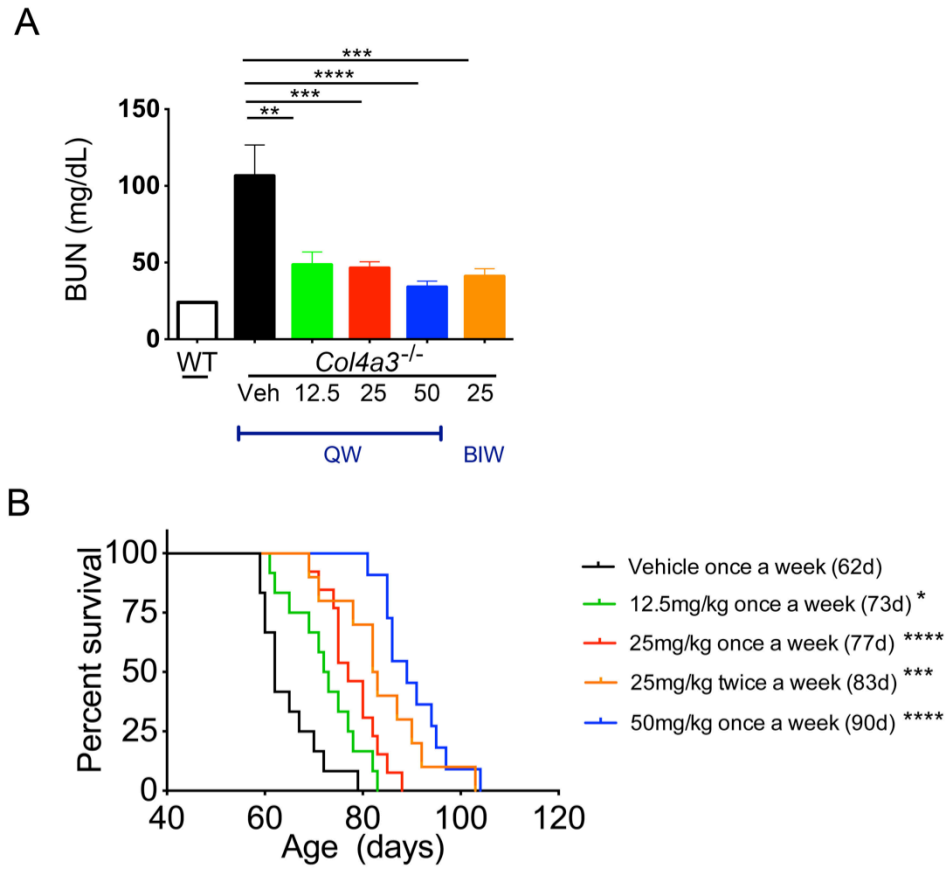

Supplemental Figure 3.

Effect of different doses of anti-miR21 on BUN levels at 8 weeks and survival in *Col4a3*$^{-/-}$ mice. (A) Graph of plasma BUN concentration at 8 weeks in response to anti-miR21 delivery subcutaneously from week 3.5 in *Col4a3*$^{-/-}$ mice, administered weekly (QW) or twice weekly (BIW). (B) Survival curves showing effect of anti-miR21 on mouse survival in response anti-miR21 delivery subcutaneously from week 3.5 in *Col4a3*$^{-/-}$ mice. Median survival () is shown (n = 12/group) (**Gehan-Breslow-Wilcoxon test for survival and 1-way ANOVA test for BUN** * $P < 0.05$, ** $P < 0.01$, *** $P < 0.001$, **** $P < 0.0001$).

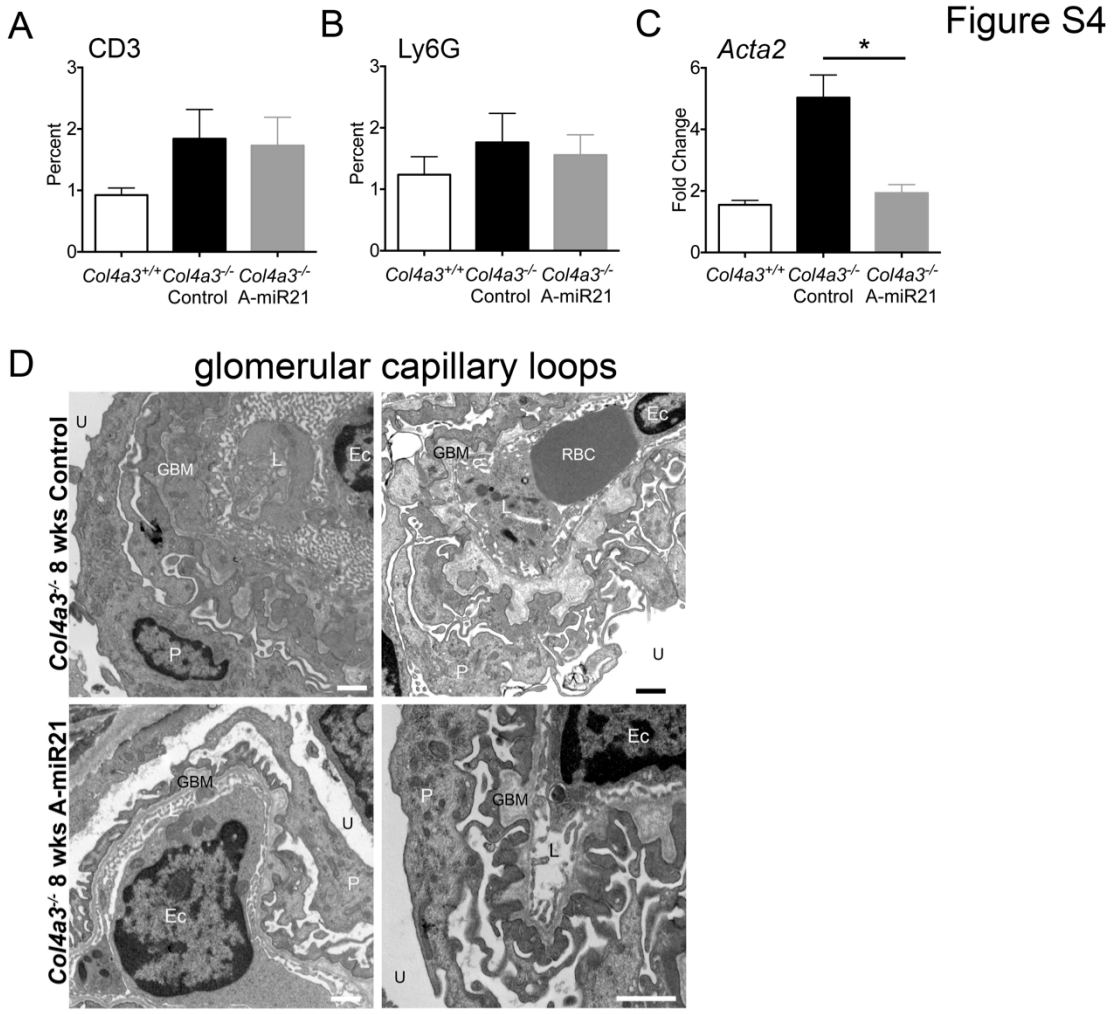

Supplemental Figure 4.

The effect of Anti-miR-21 on T cells and neutrophil numbers and Acta2 expression. (A-B) Quantification of T cells and neutrophils in kidneys at 9 weeks (C) Q-PCR quantification of *Acta2* in kidneys at 9 weeks (D) Electron micrographs of glomerular capillary loops at 8 weeks showing lumen (L), capillary wall and urinary space (U). Note that anti-miR21 treatment markedly reduces GBM thickness, reduces GBM humps and partially preserves podocyte foot processes formation (P = podocytes, RBC = erythrocyte, Ec = endothelial cell, GBM = glomerular basement membrane (bar = 500nm) (**Mann-Whitney test; *P* < 0.05)**.

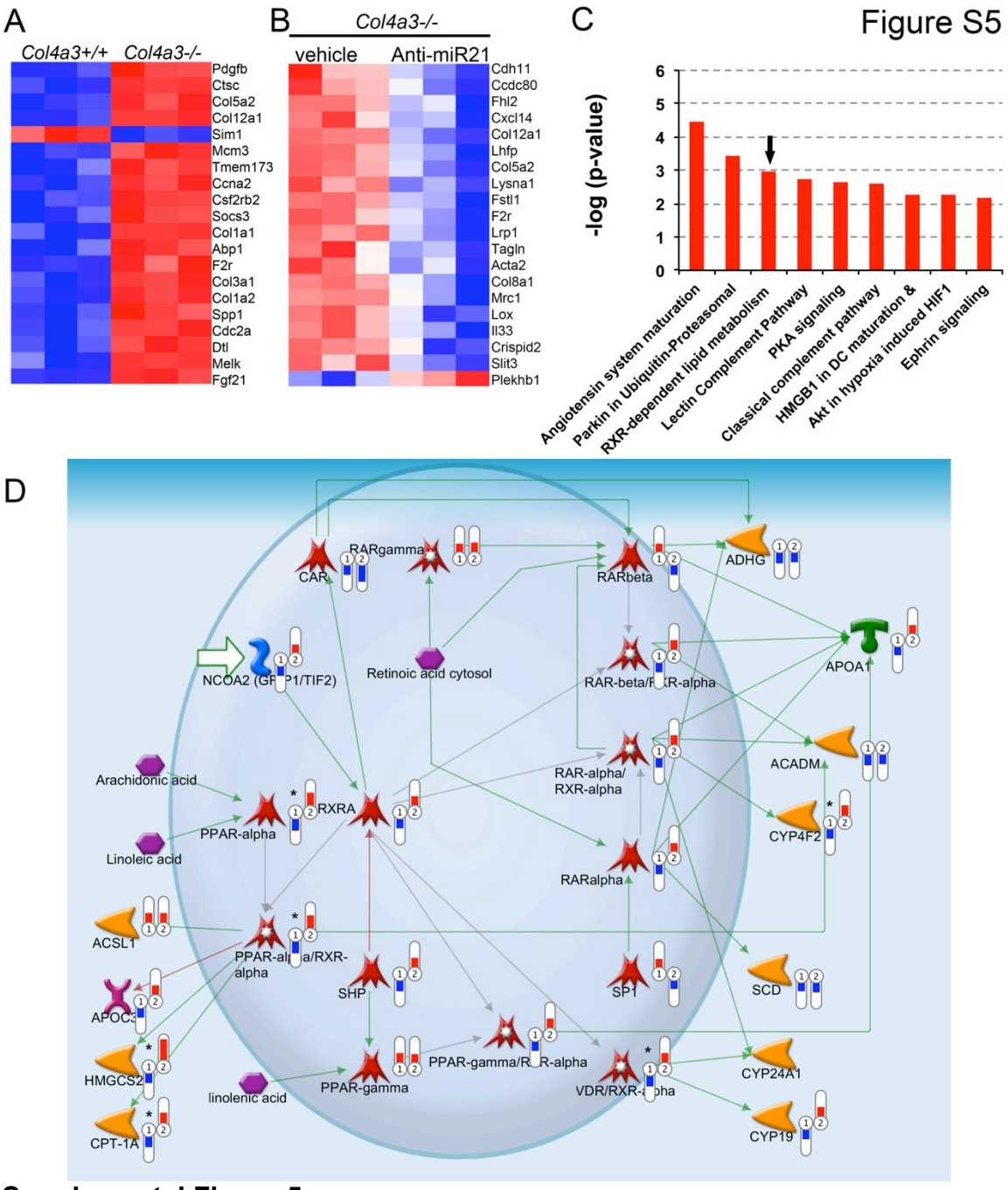

Supplemental Figure 5.

Global RNA sequencing indicates that Anti-miR-21 results in silencing of matrix gene synthesis at late timepoints and stimulation of lipid metabolism and mitochondrial functions at earlier timepoints in Alport nephropathy. (A) Heat map showing top 20 most regulated genes, quantified by whole RNA sequencing of *Col4a3*$^{-/-}$ kidneys compared to WT at 9 weeks. These include fibrillar collagens, cell cycle genes, PDGFR and FGFR signaling pathway, whereas the metabolic

transcription factor *Sim1* is highly downregulated. (B) Top 20 most statistically-significant regulated genes in *Col4a3*$^{-/-}$ kidneys treated with anti-miR-21 until 9 weeks. Anti-miR-21 results in silencing of matrix genes and fibroblast activation genes including *Col5, Col12, Acta2* and *Il33*. (C) Upregulated pathways identified through bioinformatics analysis (Metacore) of RNA transcriptomes of *Col4a3*$^{-/-}$ kidneys treated with anti-miR-21 from 3.5-5.5 weeks. Several pathways were upregulated by the action of anti-miR21, including RXR-dependent lipid metabolism PPARα, RARα and VDR (arrow). (D) Schematic of the PPARα signaling pathway at 5.5 weeks showing the genes regulated by disease (1) and by the action of anti-miR21 (2) at 5.5 weeks. red denotes upregulated genes and blue downregulated genes (* = significantly regulated). PPARα/RXRα signaling is de-repressed as identified in the pathway (RXR-dependent lipid metabolism by PPARα, RARα and VDR). *PPARα*, *RXRα* and downstream targets including *ASCL1, APOL3, HMGCS2, CPT1A* are all de-repressed. In addition other aspects of PPARα activity including RARα, and downstream target *CYP4F2* is upregulated by anti-miR-21. Transcriptionally regulated genes are shown by green connectors, transcription factors by () whereas enzymes are shown by (), transporters by () and structural proteins by (). Substrates are shown as () and interactions as (). (**Analysis performed using the Bioconductor LIMMA program n = 3/group).**

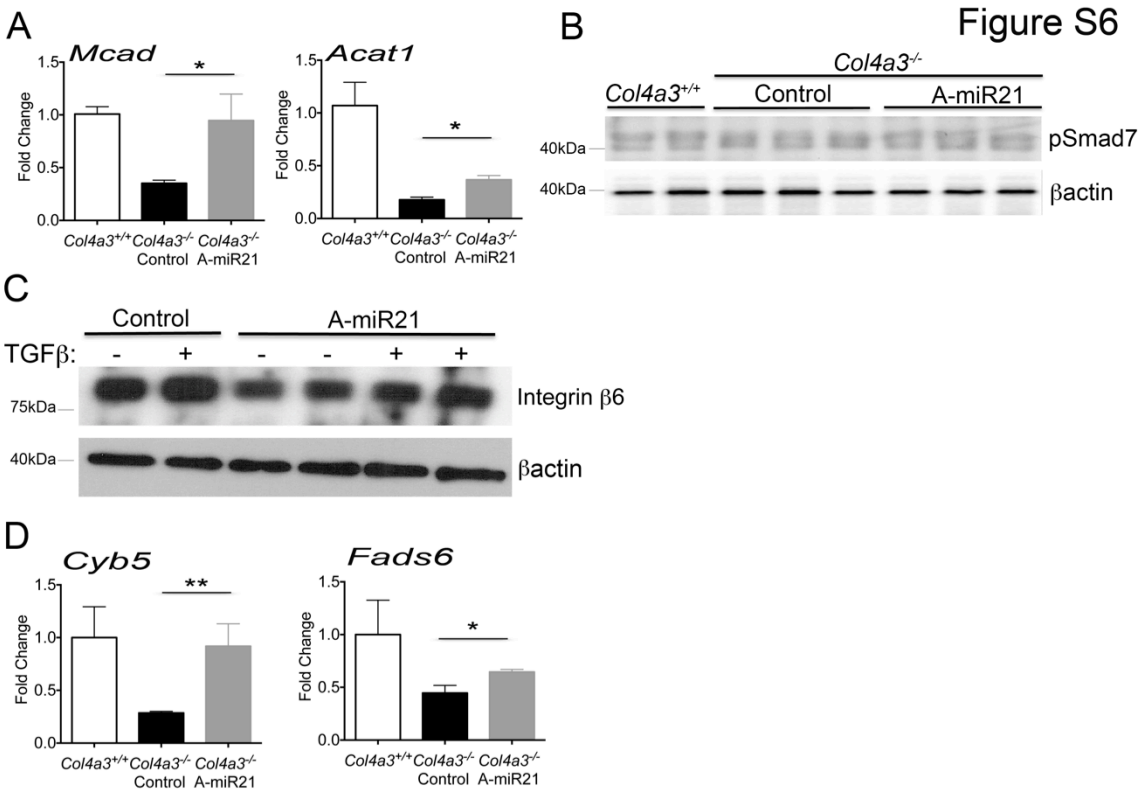

Supplemental Figure 6.

Anti-miR21 regulates fatty acid enzymes, detoxifying enzymes and TGFβ target genes but does not regulate SMAD7 activity in Alport nephropathy. (A) Graphs showing Q-PCR results from 9 week kidneys demonstrating the effect of disease and anti-miR21 administration on whole kidney levels of *Mcad* and *Acat1*. (B) Representative (of 3 separate experiments) western blot showing pSMAD-7 in whole kidney lysates at 9 weeks. (C) Representative (of 2 separate donors) western blot showing the effect of miR21 treatment and TGFβ stress on the levels of Integrin β6 in primary human PTECs. (C) Graphs of Q-PCR results for *Fads6* and *CytB* in whole kidney RNA at 9 weeks. (n=3-6/group) (**Mann-Whitney test**; * $P < 0.05$, ** $P < 0.01$)

Figure S7

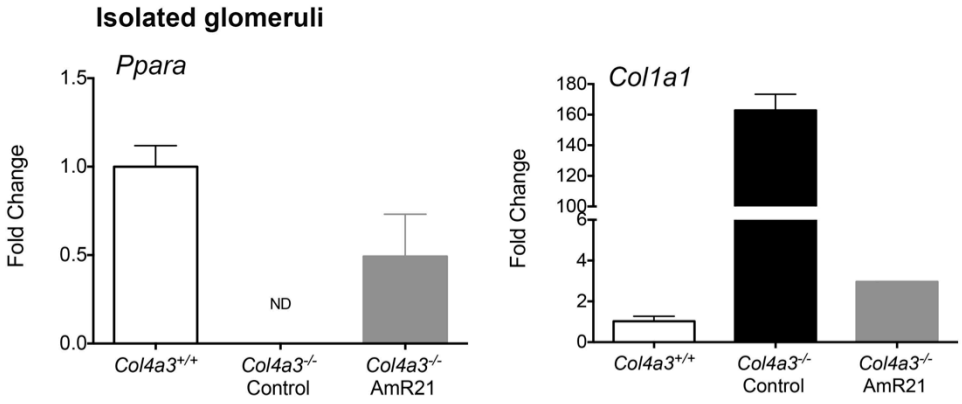

Supplemental Figure 7.

Anti-miR21 enhances glomerular Ppara and inhibits glomerular Col1a1 in the Alport nephropathy model. Graphs showing normalized Q-PCR levels for *Ppara* and *Col1a1* in 50 laser capture microdissected glomeruli per condition (n=4/group).

Figure S8

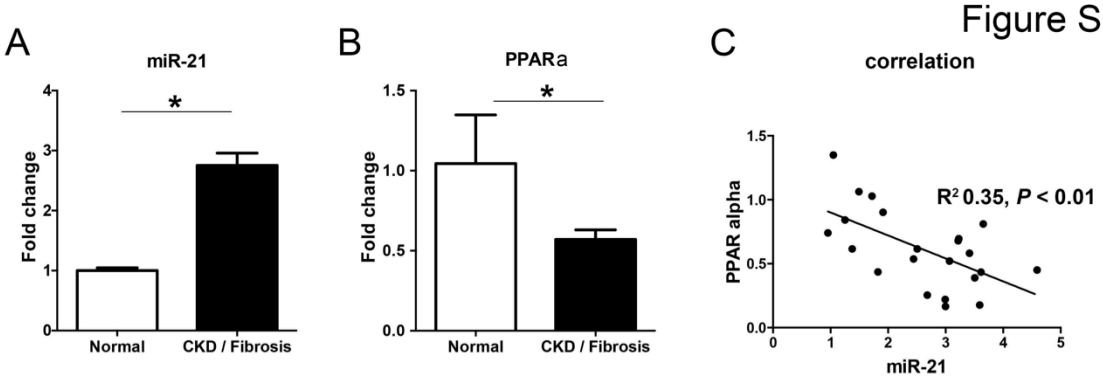

Supplemental Figure 8

Patients with chronic kidney disease of kidney transplants have elevated miR-21 levels and reduced PPARA in kidney cortex biopsies. (A) Graph showing Q-PCR results for miR-21 levels in whole RNA extracted from kidney biopsies from patients with CKD in their transplanted kidney and histologically demonstrated fibrosis, compared to patients with normal kidneys. (B) Graph showing Q-PCR results for PPARA levels in same kidney material. (C) Correlation of miR-21 and PPARA levels in individual patients (**Mann-Whitney test and linear regression for correlation curve;** n = 3 - 21/group * $P < 0.05$).

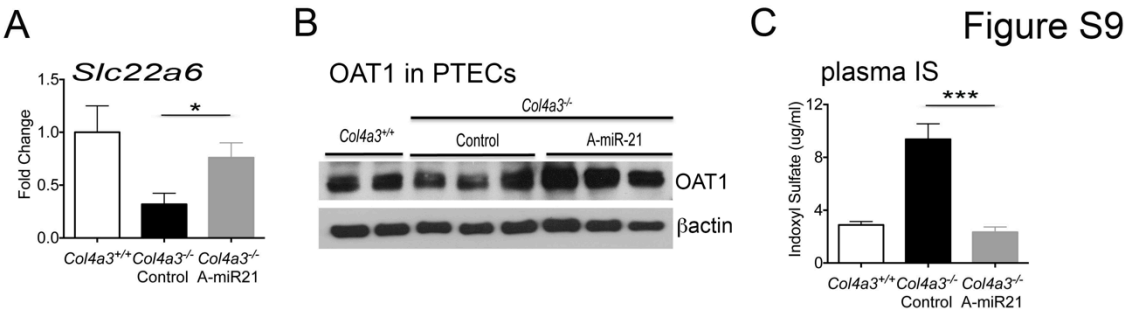

Figure S9

Supplemental Figure 9.

Anti-microRNA-21 restores OAT1 (Slc22a6) expression and tubular secretion of the uremic toxin indoxyl sulfate. (A) Graph showing Q-PCR levels for *Slc22a6* in whole kidney tissue. (B) Representative blots from 2 separate experiments showing the levels of OAT1 in primary mouse PTEC cultures from *Col4a3-/-* mice treated with anti-miR21 or control (same experiment at Figure S6B). (C) Plasma levels of the tubular secreted uremic toxin indoxyl sulfate (IS) at 9 weeks. (**Mann-Whitney test;** * $P < 0.05$, *** $P < 0.001$ n = 3-12/group).

2. Supplemental Tables

Supplemental Table 1

Validated primer sequences used to measure transcript levels by Q-RT PCR

Gene	Forward Primer	Reverse Primer
miR-21	CGGTAGCTTATCAGACTGATGTTGA	CGGTAGCTTATCAGACTGATGTTGA
Col1a1	CTGGTGAACAGGGTGTTCCT	AGAACCATCAGCACCTTTGG
Mcad	GCGAGCAGAAATGAAACTCC	AGCTCTAGACGAAGCCACGA
Acat1	TGCATAACTTCGTTCCAGGC	AGCCTTTCGCGTCTCCAT
Cyb5	AGGACTTCTTCTCCACCAGGA	GCACAAAGACAGCAAGAGCA
Fads6	CGAACTCTGCAGAAAAGGCT	CACTCACAGTGCCCTCACAG
Mpv17l	AATATGTCATCCTTCCCCTGG	CAAGGTGCTATGCGATCAGA
Slc22a6	GGCACCTTGATTGGCTATGT	CCACAGCATGGAGAGACAGA
Acta2	CTGACAGAGGCACCACTGAA	CATCTCCAGAGTCCAGCACA
Ppara	AAAGAGGCAGAGGTCCGATT	AGCAAGGTGACTTGGTCGTT
Ppargc1a	AGTCCCATACACAACCGCAG	ACCCTTGGGGTCATT TGGTG
Cpt1	AGTGGCCTCACAGACTCCAG	GCCCATGTTGTACAGCTTCC
PPARA	TCGGCGAGGATAGTTCTGGAAG	GACCACAGGATAAGTCACCGAG
PPARGC1A	CCAAAGGATGCGCTCTCGTTCA	CGGTGTCTGTAGTGGCTTGACT
GAPDH	GAGTCAACGGATTTGGTCGT	TTGATTTTGGAGGGATCTCG

3. Supplemental Experimental Procedures

Histology staining and evaluation

Kidneys were resected after systemic perfusion with ice-cold PBS. Paraffin-embedded sections of kidney fixed with neutral-buffered formalin were used for Periodic acid-Schiff, methenamine silver, and Sirius Red staining. Sclerosis index was evaluated as described (1). Briefly, in observer blinded analysis, the extent of sclerosis in 30-40 sequential glomeruli per animal in silver-stained kidney sections was determined (scarring plus capillary loop destruction) and scored from Grade 0 to 4 where 0 = none, 1 = 0-25%, 2 = 25-50%, 3 = 50-75% and 4 = >75%. Crescents were defined and quantified as described (2). Interstitial fibrosis was quantified in picrosirius red-stained paraffin sections as described (3). Epithelial injury was quantified in PAS stained kidney sections as described (4). Tissues were collected at week 8 or week 16 for EM, prepared and processed using standard methods as described (5). Grids were scanned using a Philips 410 electron microscope (Philips Export BV, Eindhoven, The Netherlands).

Immunofluorescence staining and evaluation

Mouse tissues were prepared and stained as described (6). Briefly, tissues were fixed in PLP solution for 2h and washed in 18% sucrose solution overnight prior to cryopreservation and cryosectioning (7μm). For fluorescence detection, primary antibodies against the following proteins were used for immunolabeling: αSMA-Cy3 (1:200, clone 1A4, Sigma), F4/80 (1:300 Life Technologies), CD31 (1:300, BD), WT1 (1:200, Santa Cruz), GP38 (1:200), PDGFRβ (1:400 eBioscience), CD3e-FITC, (1:100 eBioscience), Ly6G (1:400 eBioscience). Fluorescent conjugated affinity purified secondary antibody labeling (1:400-1:800, Jackson ImmunoResearch), co-labeled with DAPI, mounting with ProLong Gold/DAPI, image capture and processing were carried out as previously described using confocal imaging (7). Detection of apoptotic cells was performed using the *in situ* cell death TUNEL detection kit (Roche) on paraffin sections and quantification was performed as described (8). Quantification of cells by immunofluorescence staining was performed as described (9). In brief, sections were co-

labeled with DAPI, cells were identified by blue and green nuclear co-localization; αSMA+, and F4/80+ cells were identified by greater than 75% of the cell area immediately surrounding nuclei (detected by DAPI) staining positive with Cy3 fluorescence indicative of the antigen expression; Specific cells were counted in 10 cortical interstitial fields randomly selected at 400X magnification per mouse. Vessel fluorescence was analyzed in images at 400X magnification captured from CD31-stained sections of 10 different fields from 6 different animals. Based on fluorescence intensities ranging from 0 to 255, peritubular capillaries were distinguished from background by empirically determining threshold values that marked only blood vessels in specimens from control kidney in diseased mice. The threshold was constant for all measurements. ROS generation was detected in snap frozen kidneys by immersing freshly prepared cryosections in 2 μg/ml of Dihydroethidium (Calbiochem, Nottingham, UK) in PBS**,** using identical conditions for control and diseased tissue sections as described (10). Images were captured by confocal fluorescence microscopy (Nikon A1R Confocal, Nikon, Japan). Captured images were quantified morphometrically to measure area of fluorescent signal using Image-J.

Protein isolation and western blotting

Kidneys were homogenized in ice-cold MT Cell lysis buffer (Sigma) with proteinase inhibitors (Roche) and 1mM PMSF (Sigma) for 30seconds in a Polytron PT3000 sonicator. Samples were centrifuged for 10 min at 14000x *g* and the supernatant was taken for protein determination. Cell extracts containing 50μg of protein were prepared in SDS-sample buffer and subjected to SDS-PAGE. Proteins were transferred on to nitrocellulose paper. After the transfer, immunostaining was performed as previously described in detail. Antibodies were diluted with 1:1000 in blocking buffer. Bands were detected by the enhanced chemiluminescence (ECL) method (Pierce) as recommended by the manufacturer and luminescence captured by FluorChem-Q (ProteinSimple). The following primary antibodies were used at 1:1000 dilution to detect the specific protein: anti-Pparα (Abcam or Santa-Cruz), anti-Mpv17l (Gift, Dr. Erwin Bottinger MSSM, New York, USA), anti-OAT1 (LifeSpan BioSciences), anti-Actin, anti-integrin-α3 (Santa

Cruz), anti-collagen-α2(I) (Santa Cruz), anti-integrin-β6 (Santa Cruz), anti-pSMAD7 (R&D), anti-pSmad2/3 (Cell signaling), anti-MCAD (Life Span Biosciences) anti ACAT1 (Novus Biologicals & Abcam) and, anti-PMP70 (Milipore).

Quantitative RT-PCR

Total RNA was extracted using Trizol. Purity was determined by A260 to A280. cDNA was synthesized using oligo(dT) and random primers (iScript, BioRad). Quantitative PCR was performed using ABI machine, iTaq Universal SYBR Green Supermix (BioRad) using methods as described (8). The specific primer pairs used in Q-PCR were tested for specificity and are listed in Supplemental Table 1. *Gapdh and Hprt* were used as previously reported as the housekeeping gene (11). For RT-PCR to detect miR-21, total RNA was extracted using Trizol. For some experiments an initial reaction was performed to anneal polyA sequences to all RNA (polyA tailing) then cDNA was generated using conventional Superscript-II RT and a universal primer (Life Technologies). Q-PCR for miR-21 or the housekeeping small nucleolar RNA Sno234 was performed using the reverse universal primer specific to the annealed polyA tail and the specific forward primer to the miR-21 or Sno234 unique sequence as described (12). Alternatively miR-21 expression was measured using RT-PCR primer/probe (Life Technologies, Grand Island, NY), and the absolute levels of miR-21 expression were calculated by a standard curve that was generated using synthetic miR-21 oligonucleotides (Integrated DNA Technologies, Coralville, IA). In some experiments Laser capture microdissection (LCM) of kidney glomeruli and tubules was performed on frozen kidney tissue sections of 9wk old kidneys perfused with PBS containing RNase (Sigma Aldrich, St. Louis, MO) followed by snap freezing frozen dry ice and cutting of 20μm sections which were stained with RNase-free Hematoxylin and eosin solution (MMI, Glattbrugg, Switzerland). In some experiments, sections were treated with RNAlater (Qiagen) prior to capture. Glomeruli and tubules structures were identified morphologically with a MMI laser capture microdissection system and dissected by a laser beam. The dissected glomeruli and tubules were then collected into tubes and RNA extracted with QiaZol solution (Life Technologies, Grand Island, NY). The levels of miR-21 expression were

calculated by a standard curve that was generated using synthetic miR-21 oligonucleotides (Integrated DNA Technologies, Coralville, IA). mRNA transcripts were detected by Q-PCR.

RNA sequencing and quantification methods

Total RNA from tissue was extracted as per manufacturer's instructions (miREASY kit, Qiagen). RNA quality was assessed using BioAnalyzer (Agilent). mRNA expression profiles were determined using next-generation sequencing (NGS) on the Illumina HiSeq 2000 platform producing 50bp paired-end reads. Bowtie/TopHat suites were used to align the reads to mouse genome or transcriptome and Cufflinks or RSEM were used to quantify gene abundances. Gene level counts were then normalized with the R/Bioconductor package *limma* using the *voom*/variance stabilization method.

Kidney function evaluation

Urine albumin concentration was measured using Albuwell M kit (Exocell, Philadelphia). Urine creatinine was measured using Creatinine Liquid Reagents Assay (DIAZYME, San Diego). Urea and nitrogen levels in the serum were detected by BUN reagent set (Pointe Scientific). Urinary and blood NGAL was detected by enzyme immunoassay (Boster Immunoleader). Hydrogen peroxide was measured by OxiSelect colorimetric hydrogen peroxide assay kit (Cell Biolabs, inc). Plasma levels of indoxyl sulfate were quantified by HPLC. The analytical measurement of indoxyl sulfate in 10X dilution of 10μl of mouse plasma (triplicates) was performed by stable isotope assay dilution liquid chromatography-mass spectrometry (LC-MS). In brief, IS was separated from 20μl of protein free supernatant by reverse phase chromatography over a C18 2.1 x 100 mm WATERS T3 column. The retention time for indoxyl sulfate was 4.6 minutes. The selected ion transitions monitored by MS were 212 m/z to 132 m/z for indoxyl sulfate and 217 m/z to 137 m/z for its deuterated form. Peak areas for indoxyl sulfate and its corresponding internal standard were integrated and the data expressed as a peak area

ratio of analyte/ internal standard vs dose from which quantification of the amount of analyte in mouse plasma samples was extrapolated.

Cell culture and cell culture assays

Primary kidney proximal epithelial cells were generated and characterized as described (13), cultured in epithelial medium (4) without serum factors, from at least 3 separate donors per condition. Human PTECs were from discarded human kidneys (IRB447773EA at the University of Washington) that were digested using a collagenase based method (4) and purified by MACS column (Miltenyi) affinity for anti-Epcam antibodies attached to magnetic beads. Confluent monolayers were studied without passaging, from at least 3 separate donors. To induce cell-stress, primary PTECs were treated with TGFβ (5ng/ml) or hypoxia for 6h, 24h or 48h, and evaluated for mitochondrial and gene responses. In some experiments, cells were transfected with anti-miR21 (40nM) or mismatched oligonucleotide against a non-expressed miRNA (control) at the same concentration, and cells evaluated 24-72h later using methods described (12). Cells were evaluated for transcriptional levels and protein levels as described above. Mitochondrial content was quantified using Mitotracker and cell fluorescence quantified by confocal microscopy (14). Mitochondrial ATP production was quantified using Mitochondrial ToxGlow (Promega) and mitochondrial ROS production using Mitosox (Molecular probes) detected via confocal microscopy according to manufacturer's instructions. Primary fibroblasts/pericytes [fibro/PC] were purified and characterized from normal mouse kidney as a PDGFRβ+, Coll1a1+, CD45- population as described and myofibroblasts from kidneys 3 weeks after unilateral ischemia reperfusion injury as a Col1a1+ population as described (4) (anti-PDGFRβ antibodies gift from Bill Stallcup, Burnham Institute, UCSD, CA, USA). Cells were stained with Phalloidin-Cy3 in identical conditions. Primary human fibro/PC were purified from discarded fetal kidney tissue as the PDGFRβ+, NG2+ stromal population (IRB447773EA at the University of Washington). Cells were cultured on gelatin-coated wells in pericyte medium (4) and evaluated for transcriptional responses, stress fiber formation, migratory responses following scratch wound to the monolayer in response to TGFβ 10ng/ml using assays

described (4). In some experiments supernatants were collected and cytokine concentrations measured using multiplex analysis (Becton Dickinson). Podocytes were purified from immortomouse glomeruli, cultured on matrix and characterized as described (15), expanded at permissive temperature (32ºC) in podocyte medium and podocytes were cultured at non-permissive temperature (37ºC) for 48h prior to study.

4. Supplemental References

1. Ryu M, Mulay SR, Miosge N, Gross O, Anders H-J. Tumour necrosis factor-α drives Alport glomerulosclerosis in mice by promoting podocyte apoptosis. *J Pathol*. 2012;226(1):120–131.

2. Janssen U et al. Improved survival and amelioration of nephrotoxic nephritis in intercellular adhesion molecule-1 knockout mice. *J Am Soc Nephrol*. 1998;9(10):1805–1814.

3. Humphreys BD et al. Fate tracing reveals the pericyte and not epithelial origin of myofibroblasts in kidney fibrosis. *Am J Pathol*. 2010;176(1):85–97.

4. Ren S et al. LRP-6 is a coreceptor for multiple fibrogenic signaling pathways in pericytes and myofibroblasts that are inhibited by DKK-1. *Proc Natl Acad Sci USA*. 2013;110(4):1440–1445.

5. Alpers CE, Hudkins KL, Pritzl P, Johnson RJ. Mechanisms of clearance of immune complexes from peritubular capillaries in the rat. *Am J Pathol*. 1991;139(4):855–867.

6. Campanholle G, Ligresti G, Gharib SA, Duffield JS. Cellular mechanisms of tissue fibrosis. 3. Novel mechanisms of kidney fibrosis. *Am J Physiol, Cell Physiol*. 2013;304(7):C591–603.

7. Lin S-L, Kisseleva T, Brenner DA, Duffield JS. Pericytes and perivascular fibroblasts are the primary source of collagen-producing cells in obstructive fibrosis of the kidney. *Am J Pathol*. 2008;173(6):1617–1627.

8. Schrimpf C et al. Pericyte TIMP3 and ADAMTS1 modulate vascular stability after kidney injury. *J Am Soc Nephrol*. 2012;23(5):868–883.

9. Castano AP et al. Serum amyloid P inhibits fibrosis through Fc gamma R-dependent monocyte-macrophage regulation in vivo. *Sci Transl Med*. 2009;1(5):5ra13.

10. Kawakami T et al. Deficient Autophagy Results in Mitochondrial Dysfunction and FSGS. *J Am Soc Nephrol*. 2015 in press

11. Campanholle G et al. TLR-2/TLR-4 TREM-1 Signaling Pathway Is Dispensable in

Inflammatory Myeloid Cells during Sterile Kidney Injury. *PLoS One*. 2013;8(7):e68640.

12. Chau BN et al. MicroRNA-21 promotes fibrosis of the kidney by silencing metabolic pathways. *Sci Transl Med*. 2012;4(121):121ra18.

13. Wu C-F et al. Transforming growth factor β-1 stimulates profibrotic epithelial signaling to activate pericyte-myofibroblast transition in obstructive kidney fibrosis. *Am J Pathol*. 2013;182(1):118–131.

14. Zhang F, Fu L, Wang Y. 6-thioguanine induces mitochondrial dysfunction and oxidative DNA damage in acute lymphoblastic leukemia cells. *Mol Cell Proteomics*. 2013;12(12):3803–3811.

15. Shankland SJ, Pippin JW, Reiser J, Mundel P. Podocytes in culture: past, present, and future. *Kidney Int*. 2007;72(1):26–36.

Anti-microRNA-21 prevents progression of Alport syndrome by stimulating metabolic pathways (raw blots)

Figure 5C. PPARa BLOT

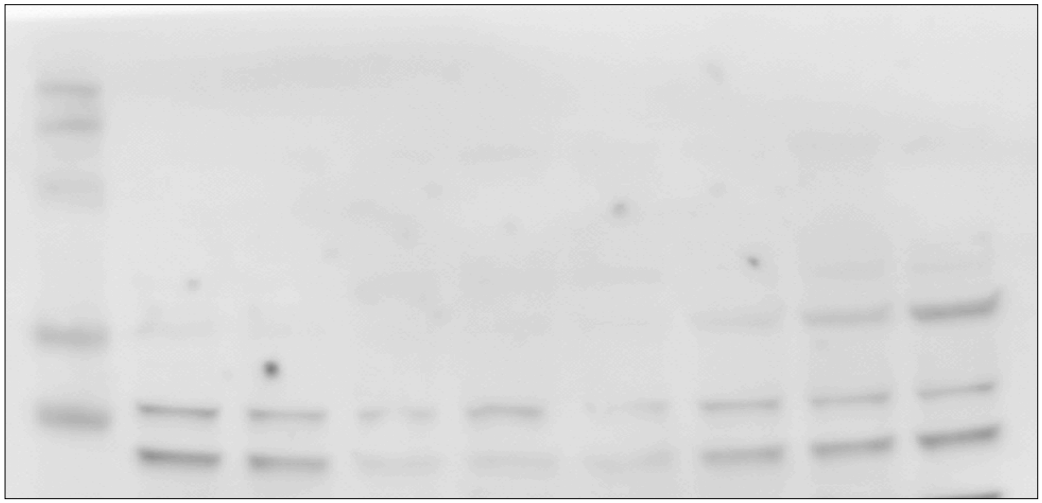

Line 1 – Ladder
Line 2 – WT Control
Line 3 – WT Control
Line 4 – Alport KO Untreated
Line 5 – Alport KO Untreated
Line 6 – Alport KO Untreated
Line 7 – Alport KO AmR21
Line 8 – Alport KO AmR21
Line 9 – Alport KO AmR21

Figure 5C. Loading control β-actin BLOT

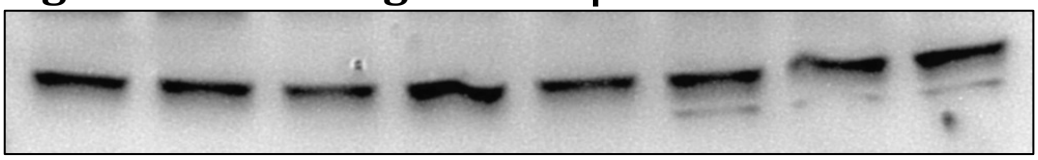

Line 1 – WT Control
Line 2 – WT Control
Line 3 – Alport KO Untreated
Line 4 – Alport KO Untreated
Line 5 – Alport KO Untreated
Line 6 – Alport KO AmR21
Line 7 – Alport KO AmR21
Line 8 – Alport KO AmR21

Figure 5D. MCAD BLOT

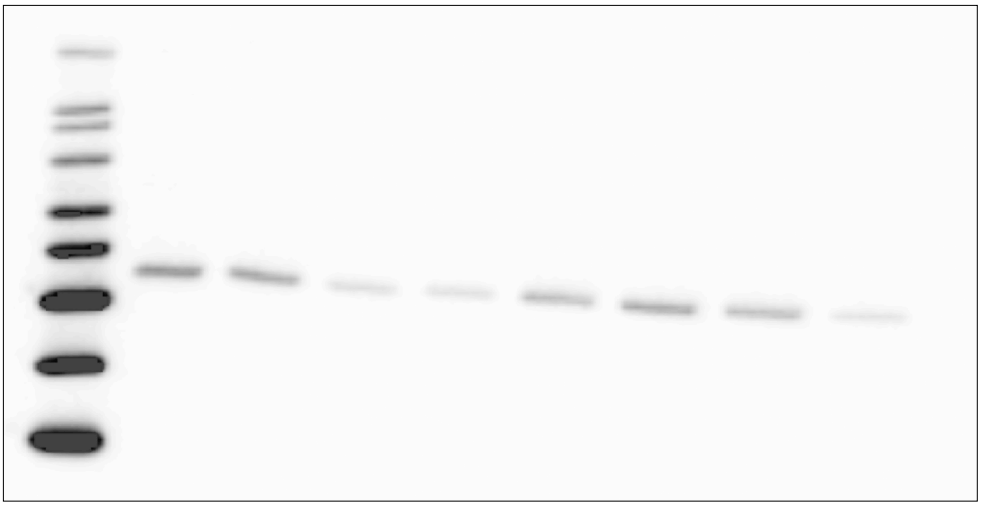

Line 1 – Ladder
Line 2 – WT Control
Line 3 – WT Control
Line 4 – Alport KO Untreated
Line 5 – Alport KO Untreated
Line 6 – Alport KO AmR21
Line 7 – Alport KO AmR21
Line 8 – Alport KO AmR21
Line 9 – Alport KO Untreated

Figure 5D. Loading control β-actin BLOT

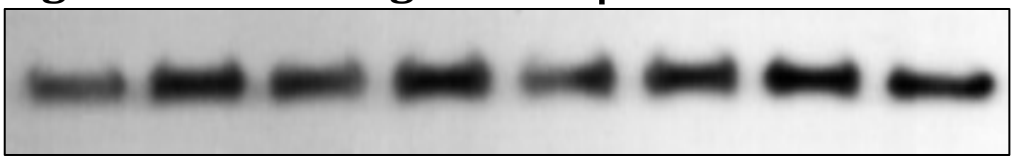

Line 1 – WT Control
Line 2 – WT Control
Line 3 – Alport KO Untreated
Line 4 – Alport KO Untreated
Line 5 – Alport KO AmR21
Line 6 – Alport KO AmR21
Line 7 – Alport KO AmR21
Line 8 – Alport KO Untreated

Figure 5E. ACAT1 BLOT

Line 1 – Ladder
Line 2 – WT Control
Line 3 – WT Control
Line 4 – Alport KO Untreated
Line 5 – Alport KO Untreated
Line 6 – Alport KO AmR21
Line 7 – Alport KO AmR21
Line 8 – Alport KO AmR21
Line 9 – Alport KO Untreated

Figure 5E. Loading control β-actin BLOT

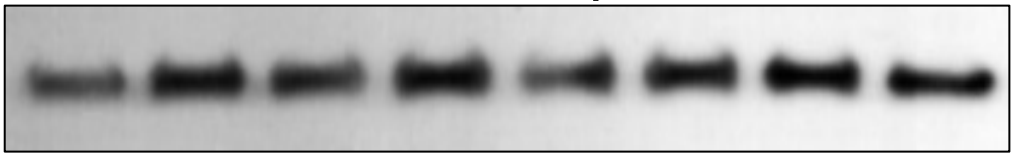

Line 1 – WT Control
Line 2 – WT Control
Line 3 – Alport KO Untreated
Line 4 – Alport KO Untreated
Line 5 – Alport KO AmR21
Line 6 – Alport KO AmR21
Line 7 – Alport KO AmR21
Line 8 – Alport KO Untreated

Figure 5F. PMP70 BLOT

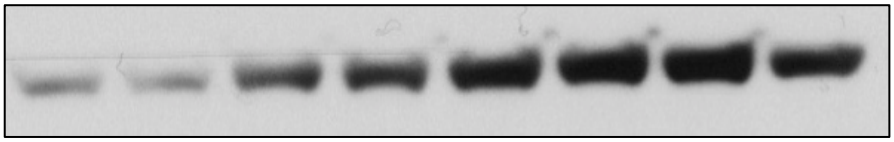

Line 1 – WT Control
Line 2 – WT Control
Line 3 – Alport KO Untreated
Line 4 – Alport KO Untreated
Line 5 – Alport KO Untreated
Line 6 – Alport KO AmR21
Line 7 – Alport KO AmR21
Line 8 – Alport KO AmR21

Figure 5F. Loading control β-actin BLOT

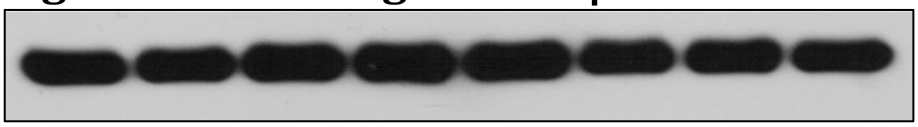

Line 1 – WT Control
Line 2 – WT Control
Line 3 – Alport KO Untreated
Line 4 – Alport KO Untreated
Line 5 – Alport KO Untreated
Line 6 – Alport KO AmR21
Line 7 – Alport KO AmR21
Line 8 – Alport KO AmR21

These blots were cut into strips, and probed as indicated above.

Figure 6G. PMP70 BLOT

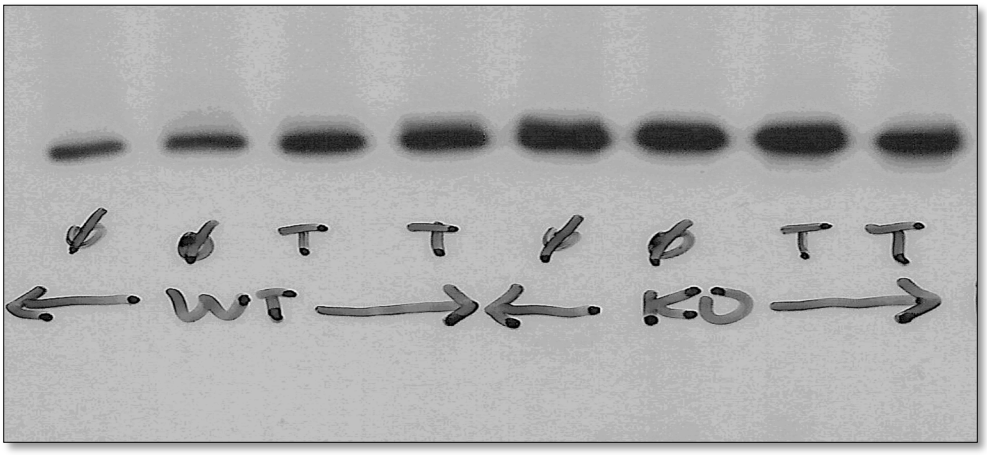

Line 1 – WT Control
Line 2 – WT Control
Line 3 – WT Control TGFb
Line 4 – WT Control TGFb
Line 5 – mRNA21-KO Control
Line 6 – mRNA21-KO Control
Line 7 – mRNA21-KO TGFb
Line 8 – mRNA21-KO TGFb

Figure 6G. Loading control β-actin BLOT

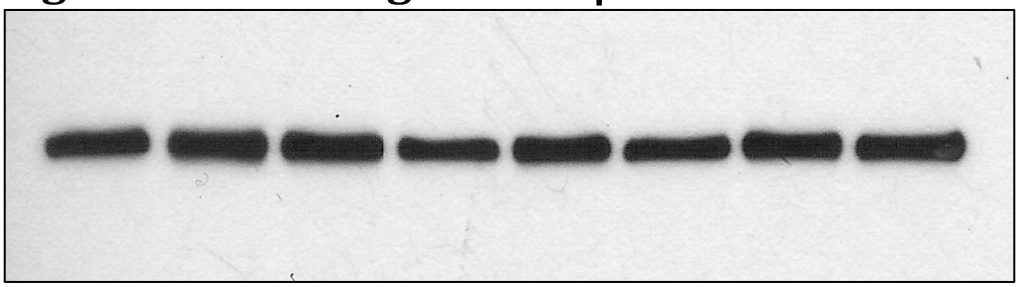

Line 1 – WT Control
Line 2 – WT Control
Line 3 – WT Control TGFb
Line 4 – WT Control TGFb
Line 5 – mRNA21-KO Control
Line 6 – mRNA21-KO Control
Line 7 – mRNA21-KO TGFb
Line 8 – mRNA21-KO TGFb

Figure 7C. MPV17L BLOT

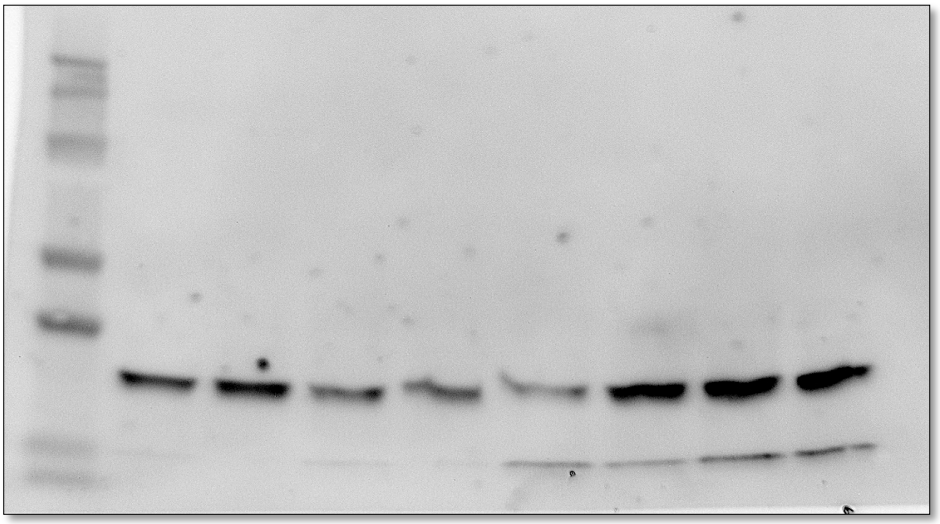

Line 1 – Ladder
Line 2 – WT Control
Line 3 – WT Control
Line 4 – Alport KO Untreated
Line 5 – Alport KO Untreated
Line 6 – Alport KO Untreated
Line 7 – Alport KO AmR21
Line 8 – Alport KO AmR21
Line 9 – Alport KO AmR21

Figure 7C. Loading control β-actin BLOT

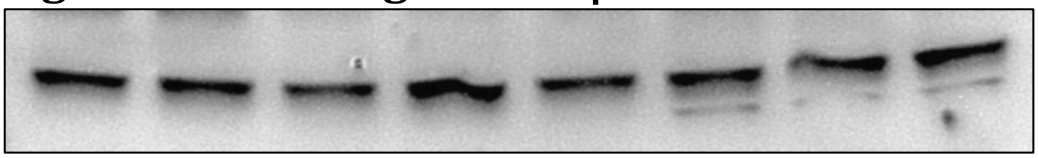

Line 1 – WT Control
Line 2 – WT Control
Line 3 – Alport KO Untreated
Line 4 – Alport KO Untreated
Line 5 – Alport KO Untreated
Line 6 – Alport KO AmR21
Line 7 – Alport KO AmR21
Line 8 – Alport KO AmR21

Figure 8J. IkB-α BLOT

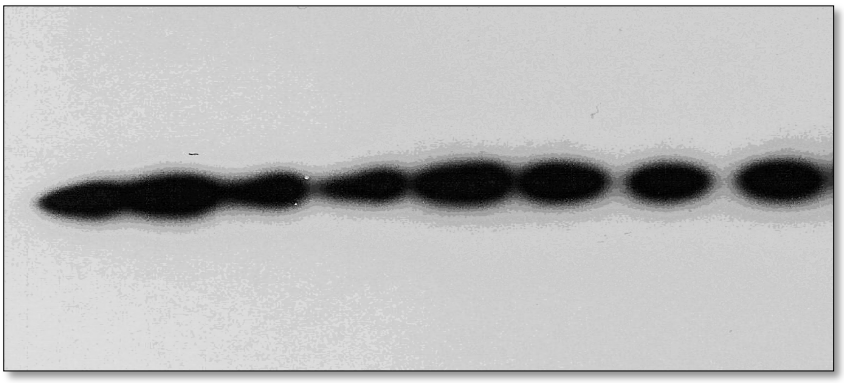

Line 1 – WT Control
Line 2 – WT Control
Line 3 – WT Control TGFb
Line 4 – WT Control TGFb
Line 5 – mRNA21-KO Control
Line 6 – mRNA21-KO Control
Line 7 – mRNA21-KO TGFb
Line 8 – mRNA21-KO TGFb

Figure 8J. Loading control β-actin BLOT

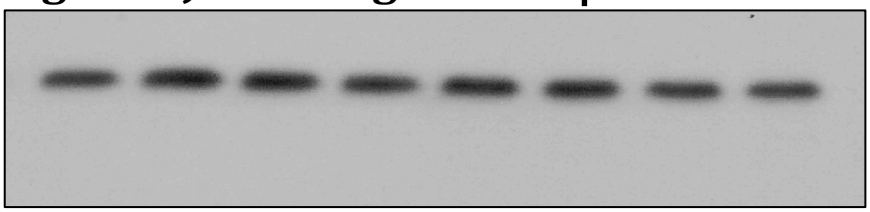

Line 1 – WT Control
Line 2 – WT Control
Line 3 – WT Control TGFb
Line 4 – WT Control TGFb
Line 5 – mRNA21-KO Control
Line 6 – mRNA21-KO Control
Line 7 – mRNA21-KO TGFb
Line 8 – mRNA21-KO TGFb

Figure 8L. Collagen α2 BLOT

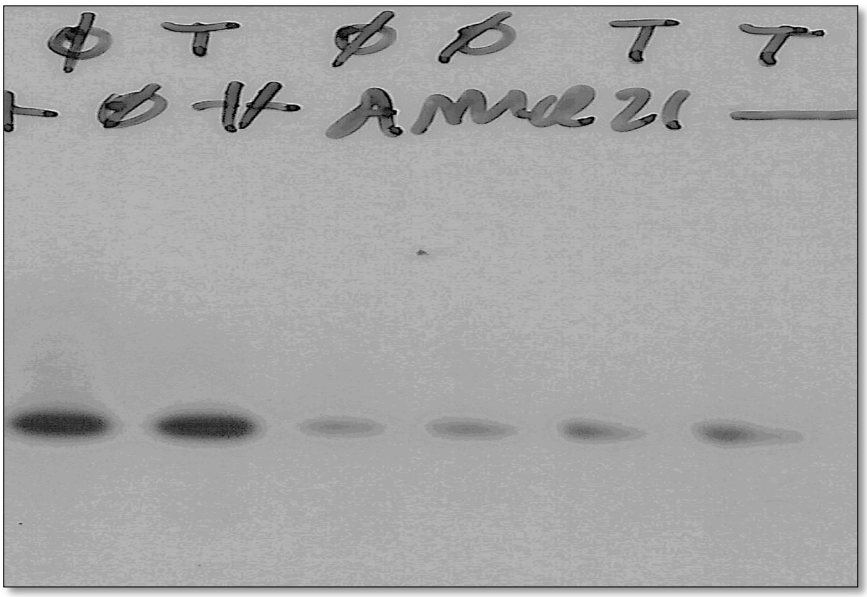

Figure 8L. Integrin α3 BLOT

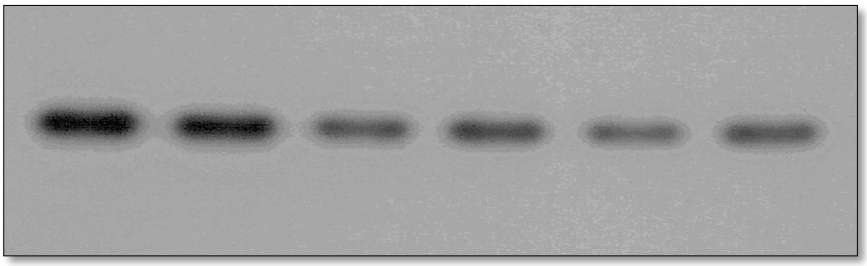

Figure 8L. Loading control β-actin BLOT

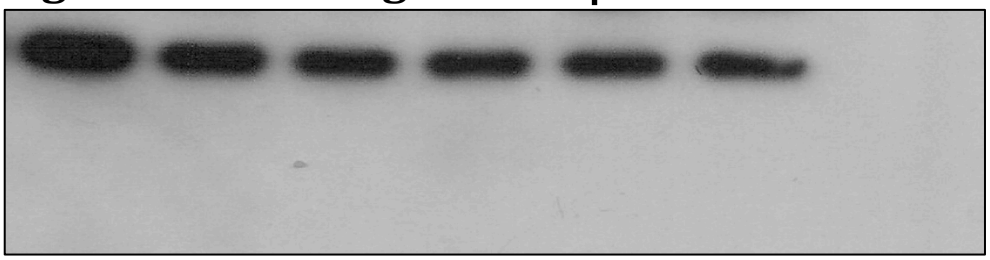

Line 1 – WT human PC Control
Line 2 – WT human PC TGFb
Line 3 – WT human PC A-mR21
Line 4 – WT human PC A-mR21
Line 5 – WT human PC A-mR21 TGFb
Line 6 – WT human PC A-mR21 TGFb

Figure S6 B. pSMAD-7 BLOT

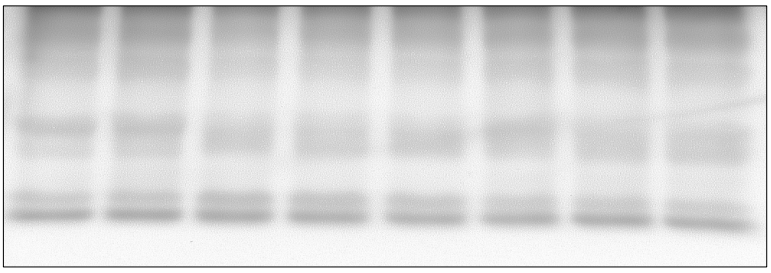

Line 1 – WT Control
Line 2 – WT Control
Line 3 – Alport KO Untreated
Line 4 – Alport KO Untreated
Line 5 – Alport KO Untreated
Line 6 – Alport KO AmR21
Line 7 – Alport KO AmR21
Line 8 – Alport KO AmR21

Figure S6 B. Loading control β-actin BLOT

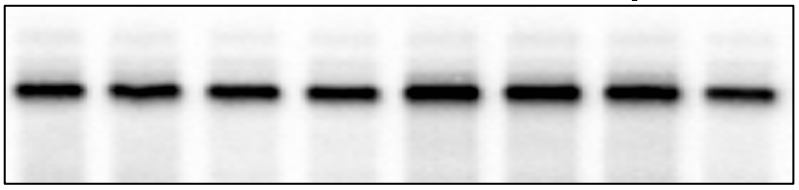

Line 1 – WT Control
Line 2 – WT Control
Line 3 – Alport KO Untreated
Line 4 – Alport KO Untreated
Line 5 – Alport KO Untreated
Line 6 – Alport KO AmR21
Line 7 – Alport KO AmR21
Line 8 – Alport KO AmR21

Figure S6 C. Integrin b6 BLOT

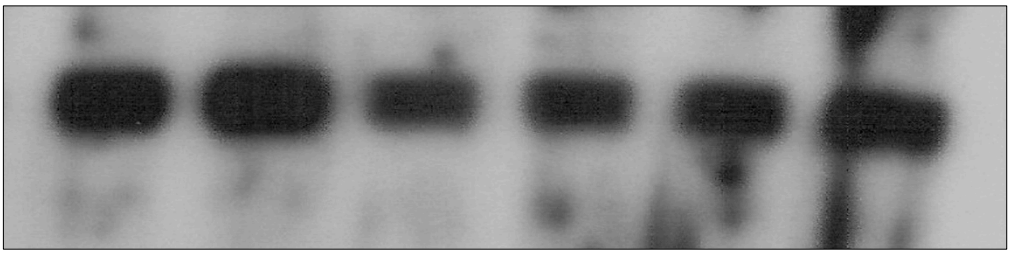

Line 1 – WT human PTEC Control
Line 2 – WT human PTEC TGFb
Line 3 – WT human PTEC A-mR21
Line 4 – WT human PTEC A-mR21
Line 5 – WT human PTEC A-mR21 TGFb
Line 6 – WT human PTEC A-mR21 TGFb

Figure S6 C. Loading control β-actin BLOT

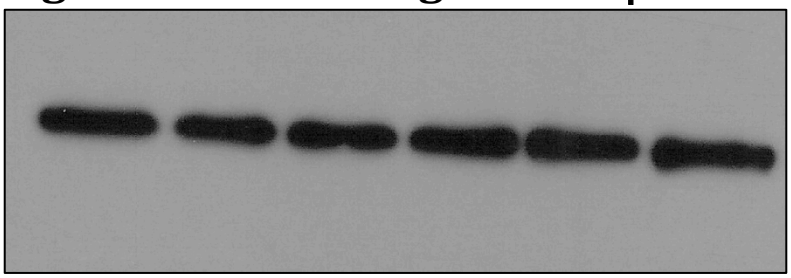

Figure S9 B. Oat-1 BLOT

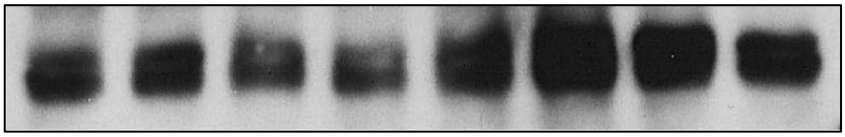

Line 1 – WT PTEC Control
Line 2 – WT PTEC Control
Line 3 – Alport KO PTEC Untreated
Line 4 – Alport KO PTEC Untreated
Line 5 – Alport KO PTEC Untreated
Line 6 – Alport KO PTEC AmR21
Line 7 – Alport KO PTEC AmR21
Line 8 – Alport KO PTEC AmR21

Figure S6 B. Loading control β-actin BLOT

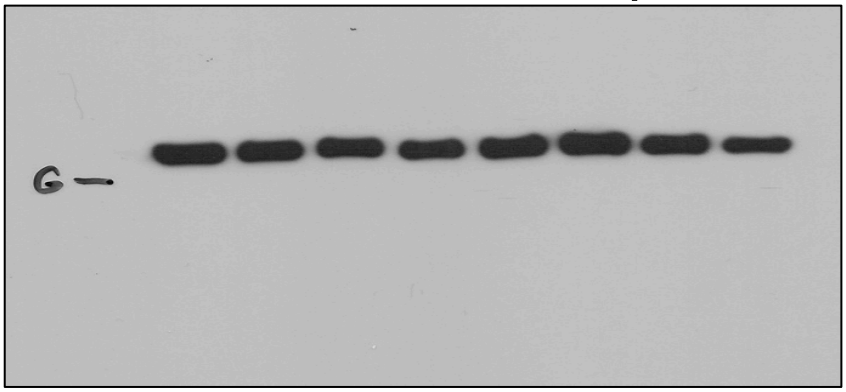

Line 1 – WT PTEC Control
Line 2 – WT PTEC Control
Line 3 – Alport KO PTEC Untreated
Line 4 – Alport KO PTEC Untreated
Line 5 – Alport KO PTEC Untreated
Line 6 – Alport KO PTEC AmR21
Line 7 – Alport KO PTEC AmR21
Line 8 – Alport KO PTEC AmR21